



**HAL**  
open science

## A squirmer across Reynolds numbers

Nicholas G. Chisholm, Dominique Legendre, Eric Lauga, Aditya S. Khair

► **To cite this version:**

Nicholas G. Chisholm, Dominique Legendre, Eric Lauga, Aditya S. Khair. A squirmer across Reynolds numbers. *Journal of Fluid Mechanics*, 2016, vol. 796, pp. 233-256. 10.1017/jfm.2016.239 . hal-01792474

**HAL Id: hal-01792474**

**<https://hal.science/hal-01792474v1>**

Submitted on 15 May 2018

**HAL** is a multi-disciplinary open access archive for the deposit and dissemination of scientific research documents, whether they are published or not. The documents may come from teaching and research institutions in France or abroad, or from public or private research centers.

L'archive ouverte pluridisciplinaire **HAL**, est destinée au dépôt et à la diffusion de documents scientifiques de niveau recherche, publiés ou non, émanant des établissements d'enseignement et de recherche français ou étrangers, des laboratoires publics ou privés.



## Open Archive TOULOUSE Archive Ouverte (OATAO)

OATAO is an open access repository that collects the work of Toulouse researchers and makes it freely available over the web where possible.

This is an author-deposited version published in: <http://oatao.univ-toulouse.fr/>  
Eprints ID: 19935

**To link to this article:** DOI: 10.1017/jfm.2016.239  
URL: <https://doi.org/10.1017/jfm.2016.239>

<p><b>To cite this version :</b> Chisholm, Nicholas G. and Legendre, Dominique and Lauga, Eric and Khair, Aditya S. <i>A squirmer across Reynolds numbers</i>. (2016) <i>Journal of Fluid Mechanics</i>, vol. 796. pp. 233-256. ISSN 0022-1120</p>
--

Any correspondence concerning this service should be sent to the repository administrator: [staff-oatao@listes-diff.inp-toulouse.fr](mailto:staff-oatao@listes-diff.inp-toulouse.fr)

# A squirmer across Reynolds numbers

Nicholas G. Chisholm<sup>1</sup>, Dominique Legendre<sup>2</sup>, Eric Lauga<sup>3</sup>  
and Aditya S. Khair<sup>1,†</sup>

<sup>1</sup>Department of Chemical Engineering, Carnegie Mellon University, Pittsburgh, PA 15213, USA

<sup>2</sup>IMFT (Institut de Mécanique des Fluides de Toulouse), Université de Toulouse, INPT-UPS,  
Allée Camille Soula, F-31400 Toulouse, France

<sup>3</sup>Department of Applied Mathematics and Theoretical Physics, Centre for Mathematical Sciences,  
University of Cambridge, Wilberforce Road, Cambridge CB3 0WA, UK

(Received 21 May 2015; revised 22 February 2016; accepted 30 March 2016;  
first published online 29 April 2016)

The self-propulsion of a spherical squirmer – a model swimming organism that achieves locomotion via steady tangential movement of its surface – is quantified across the transition from viscously to inertially dominated flow. Specifically, the flow around a squirmer is computed for Reynolds numbers ( $Re$ ) between 0.01 and 1000 by numerical solution of the Navier–Stokes equations. A squirmer with a fixed swimming stroke and fixed swimming direction is considered. We find that fluid inertia leads to profound differences in the locomotion of pusher (propelled from the rear) versus puller (propelled from the front) squirmers. Specifically, pushers have a swimming speed that increases monotonically with  $Re$ , and efficient convection of vorticity past their surface leads to steady axisymmetric flow that remains stable up to at least  $Re = 1000$ . In contrast, pullers have a swimming speed that is non-monotonic with  $Re$ . Moreover, they trap vorticity within their wake, which leads to flow instabilities that cause a decrease in the time-averaged swimming speed at large  $Re$ . The power expenditure and swimming efficiency are also computed. We show that pushers are more efficient at large  $Re$ , mainly because the flow around them can remain stable to much greater  $Re$  than is the case for pullers. Interestingly, if unstable axisymmetric flows at large  $Re$  are considered, pullers are more efficient due to the development of a Hill’s vortex-like wake structure.

**Key words:** biological fluid dynamics, propulsion, swimming/flying

---

## 1. Introduction

Swimming organisms span seven orders of magnitude in length (Gray 1968): a motile bacterium may be only a few microns across whereas a large marine animal may be several metres in length. Completely different fluid flow regimes are observed at either end of this scale (Childress 1981). The underlying flow physics are dictated by the relative strength of inertial to viscous forces within the fluid. The Reynolds number,  $Re = \rho VL/\mu$ , represents the ratio of these forces, where  $\rho$  is the fluid density,  $\mu$  is the viscosity,  $V$  is a characteristic speed, and  $L$  is a characteristic length.

† Email address for correspondence: [akhair@andrew.cmu.edu](mailto:akhair@andrew.cmu.edu)

Locomotion at macroscopic length scales is associated with large  $Re$  flows dominated by inertial forces. Roughly all swimmers between the size of a small fish ( $Re \sim 10^3$ ) and a blue whale ( $Re \sim 10^8$ ) fall into this Eulerian realm. Self-propulsion is primarily generated by reactionary forces arising from the acceleration of fluid opposite the swimming direction (Childress 1981). This is accomplished, for instance, by the motion of a fish's tail fin. The effects of viscosity are confined to thin boundary layers so long as the swimmer is streamlined in shape (Vogel 1996). Thus, fluid-mechanical analysis may be carried out using inviscid flow theory (Lighthill 1975).

In contrast, microscopic organisms fall into the Stokesian realm, where viscous forces dominate and  $Re$  is small, ranging from  $10^{-4}$  for bacteria to  $10^{-2}$  for mammalian spermatozoa (Brennen & Winnet 1977). Here, inertial mechanisms of thrust generation are unavailable; the swimming mechanics of these organisms are governed by resistive forces, where viscous thrust is balanced by viscous drag (Lauga & Powers 2009).

Lighthill (1952) and Blake (1971) introduced the spherical squirmer as a simple model for self-propulsion at small  $Re$ , intended to mimic the locomotion of organisms possessing dense arrays of motile cilia. A squirmer of radius  $a$  achieves locomotion through small, axisymmetric deformations of its surface, such that the radial and tangential velocity components on its surface in a co-moving frame are

$$v_r|_{r=a} = \sum_{n=0}^{\infty} A_n(t) P_n(\cos \theta) \quad \text{and} \quad v_\theta|_{r=a} = \sum_{n=1}^{\infty} \frac{-2}{n(n+1)} B_n(t) P_n^1(\cos \theta), \quad (1.1a,b)$$

respectively. Here,  $r$  is the distance from the origin, located at the centre of the squirmer's body,  $\theta$  is the polar coordinate measured from the direction of locomotion,  $A_n$  and  $B_n$  are time-dependent amplitudes (with units of velocity) and  $P_n$  ( $P_n^1$ ) are (associated) Legendre polynomials of order  $n$ . The direction of locomotion remains constant (at small  $Re$ ) due to the axisymmetry of the swimming 'stroke' represented by (1.1a,b), and thus the swimming velocity is  $\mathbf{U} = U\mathbf{e}_z$ , where  $\mathbf{e}_z$  is the unit vector along the swimming direction. From the requirement that the net hydrodynamic force must vanish on a steadily translating, neutrally buoyant body, the swimming speed of a squirmer in Stokes flow is  $U = (2B_1 - A_1)/3$  (Lighthill 1952). This depends only upon the first mode of each surface velocity component in (1.1a,b) and is independent of viscosity, since thrust and drag scale linearly with viscosity at  $Re = 0$ .

A reduced-order squirmer may be conceived by assuming that the surface deforms steadily and only in the tangential direction ( $A_n = 0$  and  $B_n = \text{constant}$ ). Furthermore, one may retain only the first two  $B_n$  coefficients, so that

$$v_\theta|_{r=a} = v_s(\theta) = B_1 \sin \theta + B_2 \sin \theta \cos \theta. \quad (1.2)$$

Equation (1.2) is a slip flow along the squirmer surface that vanishes at the poles ( $\theta = 0$  and  $\theta = \pi$ ). The first term in (1.2) is solely responsible for propulsion,  $U|_{Re=0} = 2B_1/3$ , and generates an irrotational velocity field decaying as  $1/r^3$ , characteristic of a potential dipole. The second term is associated with the stresslet exerted by the squirmer,  $\mathbf{S}|_{Re=0} = 4\pi\mu a^2 B_2 (3\mathbf{e}_z\mathbf{e}_z - \mathbf{I})/3$ , where  $\mathbf{I}$  is the identity tensor (Batchelor 1970; Ishikawa, Simmonds & Pedley 2006). The flow field due to this term decays as  $1/r^2$  in Stokes flow. There is no Stokeslet contribution to the velocity field because the squirmer is force-free: there is no net hydrodynamic force; drag balances thrust. Defining  $\beta = B_2/B_1$  and with  $B_1 > 0$ , squirmers are divided into pullers having  $\beta > 0$  and pushers having  $\beta < 0$  (Ishikawa, Simmonds & Pedley 2007) (figure 1). If  $|\beta| > 1$ ,

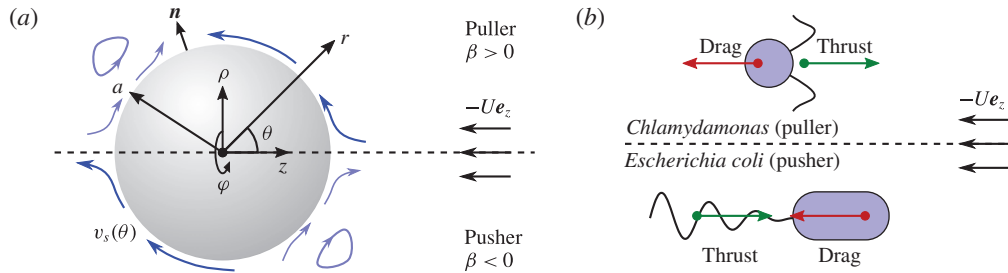


FIGURE 1. (Colour online) (a) Illustration of the flow pattern around a puller and pusher squirmer in a co-moving frame. (b) Typical examples of pusher and puller squirmers. Arrows represent the force exerted by the fluid on the swimmer body. Pullers generate thrust from the front, e.g. by using a breast-stroke-like motion such as that performed by *Chlamydomonas* (a green algae). Pushers generate thrust from the rear, e.g. by propelling themselves by rearward facing flagella as in the case of *Escherichia coli*.

there exists an intermediate point within  $0 < \theta < \pi$  at which  $v_s(\theta)$  vanishes, leading to recirculating flow behind (in front of) a puller (pusher) (Magar, Goto & Pedley 2003). The magnitude of  $\beta$  determines the amount of vorticity generation. If  $\beta = 0$ , the squirmer is ‘neutral’ and generates a potential flow, which, in fact, is a solution to the Navier–Stokes equations (NSEs) at any  $Re$ . In this sense,  $\beta$  quantifies the amount of fluid mixing by a squirmer. Importantly, the swimming speed is independent of  $\beta$  at  $Re = 0$ ; there is no coupling between vorticity generation and propulsion in Stokes flow.

Clearly, this reduced-order squirmer is a simplistic model for the locomotion of actual organisms. Nevertheless, it has been employed to examine various facets of self-propulsion in Stokes flow, including swimming in non-Newtonian fluids (Zhu *et al.* 2011; Zhu, Lauga & Brandt 2012), mixing by swimmers (Thiffeault & Childress 2010; Lin, Thiffeault & Childress 2011; Pushkin, Shum & Yeomans 2013), feeding and nutrient transport (Magar *et al.* 2003; Magar & Pedley 2005; Michelin & Lauga 2011) and hydrodynamic interactions of swimmers (Ishikawa *et al.* 2006; Drescher *et al.* 2009; Llopis & Pagonabarraga 2010). A detailed summary is provided by Pak & Lauga (2016).

Recently, the locomotion of a squirmer with stroke (1.2) was studied at non-zero  $Re$ . In particular, matched asymptotic expansions were used to compute  $U$  to  $O(Re)$  by Wang & Ardekani (2012) and to  $O(Re^2)$  by Khair & Chisholm (2014). It was found that  $U$  depends on  $\beta$  at non-zero  $Re$ : pushers ( $\beta < 0$ ) swim faster than pullers ( $\beta > 0$ ). Here, the Reynolds number is  $Re \equiv 2\rho B_1 a / (3\mu)$ . This is a result of vorticity generation, or mixing, being coupled to propulsion at finite  $Re$ . Note that the vorticity distribution around a Stokesian squirmer evolves purely via diffusion and is thus fore–aft antisymmetric. This antisymmetry precludes the generation of a net force and hence propulsion. The antisymmetry is broken at finite  $Re$  as vorticity is advected past the squirmer into a far-field inertial wake. Khair & Chisholm (2014) demonstrate that the wake structure around a squirmer is consistent with previous work on steady self-propelled bodies at non-zero  $Re$  (Afanasyev 2004; Subramanian 2010), underscoring the squirmer as a suitable reduced-order model for inertial locomotion. Additionally, Khair & Chisholm (2014) and Li & Ardekani (2014) report numerical results for the swimming speed of a squirmer for  $Re \leq 1$ , which show that the asymptotic results are of practical value in the rather limited range of  $Re \lesssim 0.2$ .

The goal of the present article is to quantify the locomotion of a spherical squirmer in the transition from viscously to inertially dominated flow. Self-propulsion in this regime has not been fully explored, especially in comparison to the Stokesian and Eulerian limits. Here, viscous and inertial forces may be simultaneously responsible for thrust and drag on a swimmer, making analysis more difficult. Specifically, we focus on intermediate values of  $Re$  that lie between 0.1 and 1000, thus bridging the gap between viscous and inertial swimming. A multitude of aquatic organisms, such as zooplankton that are on the millimetre to centimetre length scale, fall into this range and utilize a wide variety of swimming motions. The majority of past work has focused on the swimming of particular species of organisms (Jordan 1992; McHenry, Azizi & Strother 2003; Kern & Koumoutsakos 2006; Tytell *et al.* 2010; Gazzola, Van Rees & Koumoutsakos 2012). Such work undoubtedly provides valuable information on the specific locomotive strategies of these organisms. However, in contrast to past work, our objective is to quantify finite  $Re$  locomotion from a broad perspective using the simple (reduced-order) squirmer model. Specifically, through the numerical solution of the NSEs, we will determine the flow fields around pusher and puller squirmers for  $0.01 < Re < 1000$  and  $-5 \leq \beta \leq 5$ , along with their swimming speeds, power expenditure and hydrodynamic efficiency. Furthermore, we will determine the stability of the steady axisymmetric flow about a squirmer and compute the critical values of  $Re$  at which transitions to three-dimensional (3-D) and transient flow occur. A prime outcome of our work is to demonstrate that the fluid mechanics of pusher and puller squirmers are dramatically distinct at intermediate  $Re$ , in contrast to their similar locomotions at small  $Re$ .

It must be noted that the squirmer model is indeed simple in that it only considers propulsion via generation of a surface velocity, and it may not well capture the detailed flows arising from the complex geometries and locomotions of many biological swimmers. Nonetheless, its simple geometry allows examination of the essential fluid mechanics of a self-propelling body. Moreover, our results are easily compared to the classic problems of flow past a no-slip sphere and flow past an inviscid spherical bubble, which are well studied at all  $Re$ . Nonetheless, there also exist certain biological swimmers that provide reasonably close realizations of a finite  $Re$  squirmer. *Paramecium*, a ciliate 0.2 mm in size, can reach speeds of 10 mm s<sup>-1</sup> while evading threats, corresponding to  $Re \approx 2$  (Hamel *et al.* 2011). Ctenophores, the largest organisms known to use ciliary propulsion, are a few millimetres to a few centimetres in size and swim approximately one body-length per second when foraging (and faster when evading threats). Thus, the  $Re$  of the flow ranges from roughly 100 to 6000 (Matsumoto 1991). Moreover, some species of Ctenophores, such as *Pleurobrachia bachei*, have bodies that exhibit strong axial symmetry and are approximately spherical in shape (Tamm 2014). Such examples provide additional biological motivation for studying the squirmer model outside the small  $Re$  limit.

The remainder of this article is organized as follows. In §2, we present the governing equations for a self-propelled squirmer. In §3 we detail two numerical methods used for performing steady, axisymmetric and transient, 3-D simulation of flows about a squirmer, respectively. The subsequent results are presented and discussed in §4. Finally, we conclude and suggest directions for future work in §5.

## 2. Governing equations

Consider a single squirmer with a steady swimming stroke (1.2) in an unbounded incompressible Newtonian fluid (figure 1a). We normalize length by the squirmer radius  $a$ , velocity by the speed of a neutral squirmer in potential flow ( $2B_1/3$ ), time

by  $3a/(2B_1)$ , and pressure and viscous stresses by  $2B_1\mu/(3a)$ . Thus, the Reynolds number is defined as  $Re \equiv 2\rho B_1 a/(3\mu)$ . Henceforth, all quantities are dimensionless unless indicated otherwise. The fluid motion is governed by the NSEs,

$$\nabla \cdot \mathbf{v} = 0, \quad \text{and} \quad Re \frac{D\mathbf{v}}{Dt} = \nabla^2 \mathbf{v} - \nabla p, \quad (2.1a,b)$$

where  $\mathbf{v}$  is the velocity vector,  $p$  is the pressure,  $t$  is time and  $D/Dt$  represents the material derivative.

We assume that the squirmer body has a constant mass density  $\rho_b$ , equal to  $\rho$ , and is thus neutrally buoyant. If the flow about the squirmer is axisymmetric, the net hydrodynamic force perpendicular to the squirmer's axis (taken as the  $z$ -axis of an attached Cartesian frame) and the net hydrodynamic torque vanish. Thus, the squirmer does not rotate and maintains a straight-line path. The remaining  $z$ -component of the hydrodynamic force  $F_z$  is equal to the mass times acceleration of the squirmer body in the  $z$ -direction,

$$Stk \frac{dU}{dt} = F_z = \int_S (\mathbf{n} \cdot \boldsymbol{\sigma} \cdot \mathbf{e}_z) dS, \quad (2.2)$$

where  $U$  is the swimming speed,  $S$  represents the spherical squirmer surface with outer unit normal  $\mathbf{n}$  and  $\boldsymbol{\sigma} = -p\mathbf{I} + \nabla \mathbf{v} + (\nabla \mathbf{v})^T$  is the stress tensor. The Stokes number,  $Stk = Re\rho_b/\rho$ , is equal to  $Re$  because  $\rho = \rho_b$ . This force will vanish when the flow is at steady state and the squirmer translates with a steady velocity. Therefore, a steady squirmer in steady axisymmetric flow is force-free and torque-free.

However, the spherical squirmer is a bluff object; the steady axisymmetric flow around it may become unstable beyond a critical value of  $Re$ , yielding to 3-D and/or unsteady flow. This leads to the production of instantaneous lift forces perpendicular to the squirmer's axis and instantaneous hydrodynamic torques that result in lateral motion and rotation of the squirmer's body, respectively. Here, for simplicity, forces and torques are externally applied to the squirmer to keep its direction and orientation constant and along the  $z$ -axis during our computations, although the speed is allowed to vary according to (2.2). Thus, the squirmer is not fully free-swimming but rather constrained to follow a straight-line path. This is a logical first step before considering the more complicated paths of motion that would arise if the squirmer trajectory were to be unconstrained. For instance, the transitions in flow that occur for a freely rising or sinking body, and the values of  $Re$  at which they occur, are closely related to those that take place in the flow past an analogous fixed body (Horowitz & Williamson 2010; Ern *et al.* 2012). Thus, we expect that our study of a squirmer constrained to a single direction of swimming will be relevant to a fully free-swimming squirmer. Indeed, the two problems are identical in the regime of axisymmetric flow and only differ when such flow destabilizes. Although it is not considered here, note that the path of motion of a fully free squirmer could be computed via a force balance (in all directions) and an angular momentum balance on the squirmer body, similar to the computation of the paths of freely rising or falling bodies (Ern *et al.* 2012).

### 3. Numerical methods

Two numerical schemes were employed to compute the flow field around a squirmer for  $-5 \leq \beta \leq 5$  and  $0.01 \leq Re \leq 1000$ . The first assumes steady axisymmetric flow where the steady-state swimming speed  $U$  is that at which  $F_z$  in (2.2) vanishes. The second considers fully 3-D, transient flow, in which case  $U = U(t)$  is given by integrating (2.2) via a time-stepping procedure.



### 3.1. Computation of steady axisymmetric flow

We convert the NSEs into stream function–vorticity form. From (2.1a,b), the steady vorticity transport equation is

$$Re[(\mathbf{v} \cdot \nabla)\boldsymbol{\omega} - (\boldsymbol{\omega} \cdot \nabla)\mathbf{v}] = \nabla^2 \boldsymbol{\omega}, \quad (3.1)$$

where  $\boldsymbol{\omega} = \nabla \times \mathbf{v}$  is the vorticity vector. A stream function  $\psi$  is defined in cylindrical coordinates, such that

$$v_\rho = -\frac{1}{\rho} \frac{\partial \psi}{\partial z}, \quad \text{and} \quad v_z = \frac{1}{\rho} \frac{\partial \psi}{\partial \rho}, \quad (3.2a,b)$$

where  $\rho$  is the distance from the  $z$ -axis and  $v_\rho$  and  $v_z$  represent the fluid velocity components.

Combining (3.2a,b) with (3.1) gives

$$Re \left( \left( \frac{\partial(\psi, \omega)}{\partial(r, z)} \right) + \frac{\omega}{r^2} \frac{\partial \psi}{\partial z} \right) = \nabla^2 \omega - \frac{\omega}{r^2}, \quad (3.3)$$

where  $\omega$  is the component of  $\boldsymbol{\omega}$  in the azimuthal direction  $\varphi$  about the  $z$ -axis; the other ( $\rho$  and  $z$ ) components of  $\boldsymbol{\omega}$  vanish by symmetry. Expressing  $\omega$  in terms of  $\psi$  gives

$$\omega \rho = -E^2 \psi, \quad \text{where} \quad E^2 \equiv \rho \frac{\partial}{\partial \rho} \left( \frac{1}{\rho} \frac{\partial}{\partial \rho} \right) + \frac{\partial^2}{\partial z^2}. \quad (3.4)$$

Equations (3.3) and (3.4) are coupled partial differential equations, with the former being nonlinear. These may be simultaneously solved for the scalar quantities  $\psi$  and  $\omega$  to give the flow field given appropriate boundary conditions.

In a co-moving frame, the squirmer surface ( $r=1$ ) is a streamline with tangential velocity given by (1.2). Thus,  $\psi|_{r=1} = 0$  and  $[\nabla \psi \cdot \mathbf{n}]_{r=1} = v_s \sin \theta = 3 \sin^2 \theta (1 + \beta \cos \theta)/2$ . The values of  $\beta$  and  $Re$  are specified constants, so the swimming stroke is represented as a fixed boundary condition. By axisymmetry,  $\psi|_{\rho=0} = 0$  and  $\omega|_{\rho=0} = 0$  on the  $z$ -axis. Finally, the flow is uniform in the far-field, so  $\psi|_{r \rightarrow \infty} = -U\rho^2/2$  and  $\omega|_{r \rightarrow \infty} = 0$ .

A spectral element method (Karniadakis & Sherwin 2005) was used to spatially discretize (3.3), (3.4) and the boundary conditions. The shape functions were defined as a tensor product of  $N$ th order Lagrange polynomials supported at the  $N + 1$  Gauss–Lobatto integration points over the square  $[-1, 1]^2$  parametric space of each quadrilateral element. Integration over each element was carried out using the corresponding Gauss–Lobatto quadrature rule to produce a system of nonlinear algebraic equations. This system was solved iteratively using Newton–Raphson iteration. Iteration was terminated when the  $L^2$ -norm of the relative errors in  $\psi$  and  $\omega$  over all discretization points was reduced below  $10^{-6}$ .

The spatial domain was discretized into high-order computational grids using the software package ‘Gmsh’ (Geuzaine & Remacle 2009). Three different grids were used depending on the value of  $Re$ . For  $Re \leq 0.1$ , a polar grid extending to  $R_\infty = 1000$  and consisting of  $9 \times 9$  node quadrilateral elements was used. The elements were distributed evenly in the  $\theta$ -direction ( $N_\theta = 10$ ) and progressed geometrically outward in the  $r$ -direction ( $N_r = 20$ ). A similar grid was used for  $0.1 \leq Re \leq 10$ , with  $R_\infty = 100$  (figure 2a). For  $Re > 10$ , a different mesh was used to provide better resolution in the



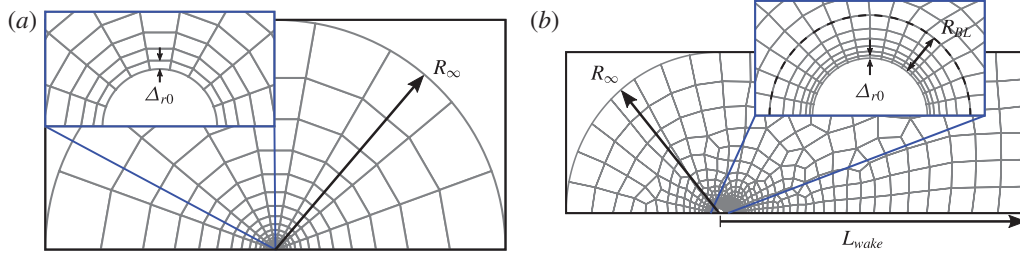


FIGURE 2. (Colour online) Structured polar grids (a) were used for both axisymmetric and 3-D (by revolving them azimuthally) computations of the flow. For axisymmetric computations with  $Re > 10$ , a different mesh (b) was used with greater resolution in the wake of the squirmer to more accurately resolve the details of the flow in this region.

squirmer wake. Here, a boundary layer grid was used along the squirmer surface, with  $N_r = 10$  and  $N_\theta = 51$ , extending  $R_{BL} = 0.25$  radii from the squirmer surface (here the subscript *BL* stands for boundary layer). The radial grid size grew geometrically with  $r$ , and was initially  $\Delta_{r0} = 0.01$  at the squirmer surface. The remainder of the grid was unstructured, with upstream boundaries extending to  $R_\infty = 32$ , and a rectangular wake region extending a distance of 100 radii behind the squirmer (figure 2b). The far-field boundary conditions were enforced at the exterior boundary of the mesh. We refer the reader to the [Appendix](#) for details on grid convergence.

The far-field boundary condition of uniform, oncoming flow cannot be directly applied because the steady-state swimming speed  $U$  is unknown *a priori*. Since the flow is assumed to be steady and axisymmetric, we instead enforce that  $F_z$  is equal to zero. Expressing (2.2) in terms of  $\omega$  for an axisymmetric flow field gives (Khair & Chisholm 2014)

$$F_z = Re \frac{\pi}{2} \int_0^\pi v_s^2 \sin(2\theta) d\theta + \pi \int_0^\pi \left( \frac{\partial(r\omega)}{\partial r} - 2\omega \right) \sin^2 \theta d\theta. \quad (3.5)$$

A secant method was used to iteratively compute the value of  $U$  at which (3.5) vanishes. At each iteration, the flow is solved with  $U = U^{(n)}$ , where  $n$  is the iteration number, and (3.5) is evaluated to give  $F_z^{(n)}$ . An improved estimate for  $U$  is given by linear interpolation:  $U^{(n+1)} = (U^{(n)} F_z^{(n-1)} - U^{(n-1)} F_z^{(n)}) / (F_z^{(n-1)} - F_z^{(n)})$ . Iteration was terminated when  $|U^{(n)} - U^{(n-1)}|$  was reduced below  $10^{-5}$ .

Computations for each value of  $\beta$  were started initially with  $Re = 0.01$ . Two initial guesses of the swimming speed are required, which were made as  $U^{(0)} = 0.99$  and  $U^{(1)} = 1.01$ , since  $U$  is close to unity at small  $Re$ . An initial guess for the stream function and vorticity fields of uniformly zero was sufficient for convergence of the computed flow in this case. A simple continuation strategy was employed by incrementally increasing  $Re$ . Initial guesses for  $U$  and the flow field at a given  $Re$  were supplied by using the values computed at the last largest values of  $Re$  for which a converged solution was successfully reached.

### 3.2. Computation of unsteady 3-D flows

Unsteady 3-D flows were explored using the JADIM code described in detail in Magnaudet, Rivero & Fabre (1995) and Legendre & Magnaudet (1998). The JADIM code has been extensively used and validated in previous studies concerning the

3-D flow dynamics of spheroidal and disk-shaped bodies with no-slip (solid) or slip (bubble) surfaces in uniform, shear or turbulent flows (see e.g. Legendre & Magnaudet 1998; Merle, Legendre & Magnaudet 2005; Legendre, Merle & Magnaudet 2006; Hallez & Legendre 2011). In particular, the wake transition from axisymmetric to 3-D flow for a fixed body has been considered in Mougin & Magnaudet (2001), Magnaudet & Mougin (2007) and Fabre, Auguste & Magnaudet (2008). In the case of a sphere, a first bifurcation resulting in loss of axial symmetry in the flow is detected at a critical Reynolds number (based on the sphere radius and speed of translation  $U$ ) of  $Re_U^{(c1)} = 105$ , in agreement with linear stability analysis (Natarajan & Acrivos 1993) and previous numerical studies (Johnson & Patel 1999; Tomboulides & Orszag 2000). A second (Hopf) bifurcation is observed at  $Re_U^{(c2)} = 135$ , leading to time-dependent flow, which is also in good agreement with previous numerical findings (Johnson & Patel 1999; Tomboulides & Orszag 2000), according to which the Hopf bifurcation lies in within the range  $135 < Re_U^{(c2)} < 137$ . In Magnaudet & Mougin (2007), the vortex shedding process for a sphere at  $Re_U = 150$  corresponds to a Strouhal number of  $St_U = fa/U = 0.0665$ , where  $f$  is the dimensional frequency of vortex shedding. This falls within 2–3% of that reported by Johnson & Patel (1999) and Tomboulides & Orszag (2000) for the same  $Re$ .

Briefly, the JADIM code solves the incompressible NSEs (2.1*a,b*) in terms of velocity and pressure variables. The spatial discretization employs a staggered grid on which the equations are integrated using a second-order accurate finite-volume method. Fluid incompressibility is satisfied after each time step by solving a Poisson equation for an auxiliary potential. Time advancement is achieved through a second-order accurate Runge–Kutta/Crank–Nicholson algorithm. At each time step, the swimming speed  $U$  is updated by integrating (2.2). For each simulation, the squirmer was started from rest with swimming stroke (1.2) and allowed to accelerate. Simulations were terminated after a steady time-averaged value of the swimming speed was reached.

A polar grid extending to  $R_\infty = 150$  and rotated around the  $z$ -axis was used for computation (figure 2*a*). Nodes were distributed uniformly in the  $\theta$ -direction and in a geometric progression in the  $r$ -direction. The effect of the number of nodes ( $N_r = 150$  along the radial direction,  $N_\theta = 250$  along the polar direction and  $N_\phi = 64$  along the azimuthal direction), as well as  $R_\infty$  and the radial grid size  $\Delta_{r,0} = 0.001$  at the body surface, were checked in order to ensure grid independence of the results (see the Appendix).

The transition from steady axisymmetric to unsteady 3-D flow was investigated by running the simulation for a given period of time while allowing numerical error to perturb the initially axisymmetric flow profile. If the flow is unstable for a given  $\beta$  and  $Re$ , such perturbations are expected to grow over time, resulting in a flow field that is potentially 3-D and/or unsteady. Such is the case for a no-slip sphere in uniform flow, where distinct axisymmetric, steady 3-D and unsteady 3-D flow regimes are respectively encountered as  $Re$  is increased (Natarajan & Acrivos 1993; Tomboulides & Orszag 2000). Specifically, simulations were performed with  $Re$  increased in coarse increments until a transition, if one occurred, was identified. Then,  $Re$  was increased in finer increments within the interval in which the transition occurred. This process was repeated until a satisfactory estimate of the critical transition  $Re$  was procured. The simulation time was increased as the critical  $Re$  of transition was approached, as it generally required longer times for perturbations to grow and hence for the flow to reach a final transitioned state.

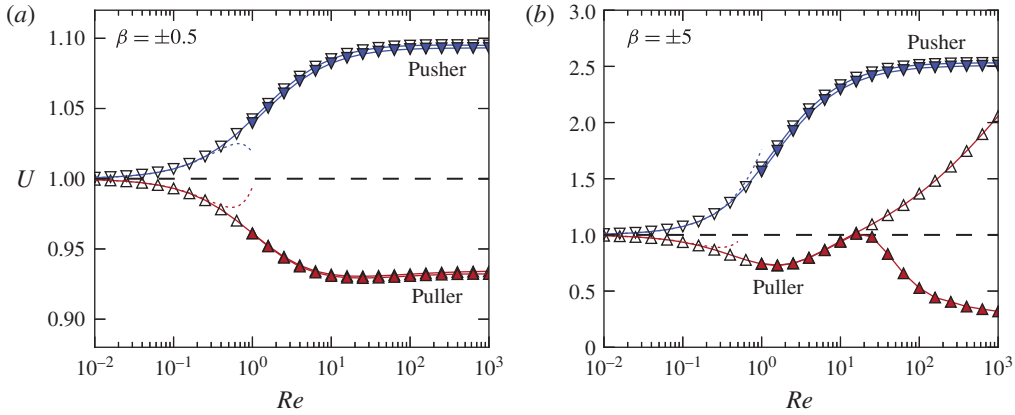


FIGURE 3. (Colour online) Swimming speed,  $U$ , normalized by  $2B_1/3$ , for  $\beta = \pm 0.5$  (a) and  $\pm 5$  (b). The ‘ $\nabla$ ’ markers represent pushers and the ‘ $\triangle$ ’ markers represent pullers. Hollow markers represent steady axisymmetric solutions, and filled markers represent unsteady 3-D solutions. We follow these conventions for the remainder of the article. The dashed line represents the speed of a neutral ( $\beta = 0$ ) squirmer. For a  $\beta = +5$  puller, the steady axisymmetric flow destabilizes at  $Re \approx 20$ , and hence the steady axisymmetric and unsteady 3-D solutions diverge. Time averages of  $U$  are taken in the case of unsteady flow. Dotted lines show the asymptotic result of Khair & Chisholm (2014) for  $U$  to  $O(Re^2)$ .

## 4. Results and discussion

### 4.1. Swimming speed of a squirmer

The calculated swimming speed  $U$  versus  $Re$  of a squirmer with  $\beta = \pm 0.5$  and  $\pm 5$  is shown in figure 3. There,  $U$  is normalized by  $2B_1/3$ , which is the swimming speed at  $Re = 0$  for all  $\beta$ , or the swimming speed of a neutral squirmer at arbitrary  $Re$ . At  $Re = 0$ ,  $U$  is independent of  $\beta$  because the equations governing the flow are linear. Thus, the two terms in the swimming stroke (1.2) contribute to the flow field independently; only the first (treading) term generates propulsion, while the second only produces vorticity. This is not the case as  $Re$  is increased from zero: pushers (pullers) monotonically increase (decrease) in speed if  $Re \lesssim O(1)$ , in agreement with results from asymptotic analyses (Wang & Ardekani 2012; Khair & Chisholm 2014). The increase or decrease in swimming speed is amplified as  $|\beta|$  increases. However, as  $Re$  is increased beyond an  $O(1)$  value, significantly different behaviour of pushers versus pullers is observed. For all pushers and pullers with  $\beta < 1$ ,  $U$  continues to vary monotonically with increasing  $Re$ , eventually reaching a terminal value. The computed swimming speed is nearly identical for axisymmetric and 3-D computations, suggesting that there is no departure from steady axisymmetric flow. In contrast, a non-monotonic trend is observed for pullers with  $\beta > 1$ , and no limiting value for  $U$  is apparent up to  $Re = 1000$ . Moreover, the axisymmetric and 3-D computations give drastically different results, suggesting the destabilization of the axisymmetric steady flow (see § 4.3 for more detail). We remind the reader that  $Re$  for a squirmer is defined as  $2\rho B_1 a / (3\mu)$ , in contrast to the Reynolds number based on the translational speed  $U$ , which we denote  $Re_U = \rho U a / \mu$ . Note that  $Re$  and  $Re_U$  are the same order of magnitude since  $U \sim O(1)$ .

Distinct contributions to the thrust and drag on a squirmer are provided by the two terms on the right-hand side of (3.5). The first term, which equals  $8\pi Re\beta/15$  after integration, depends solely on the swimming stroke and vanishes when  $Re = 0$ .

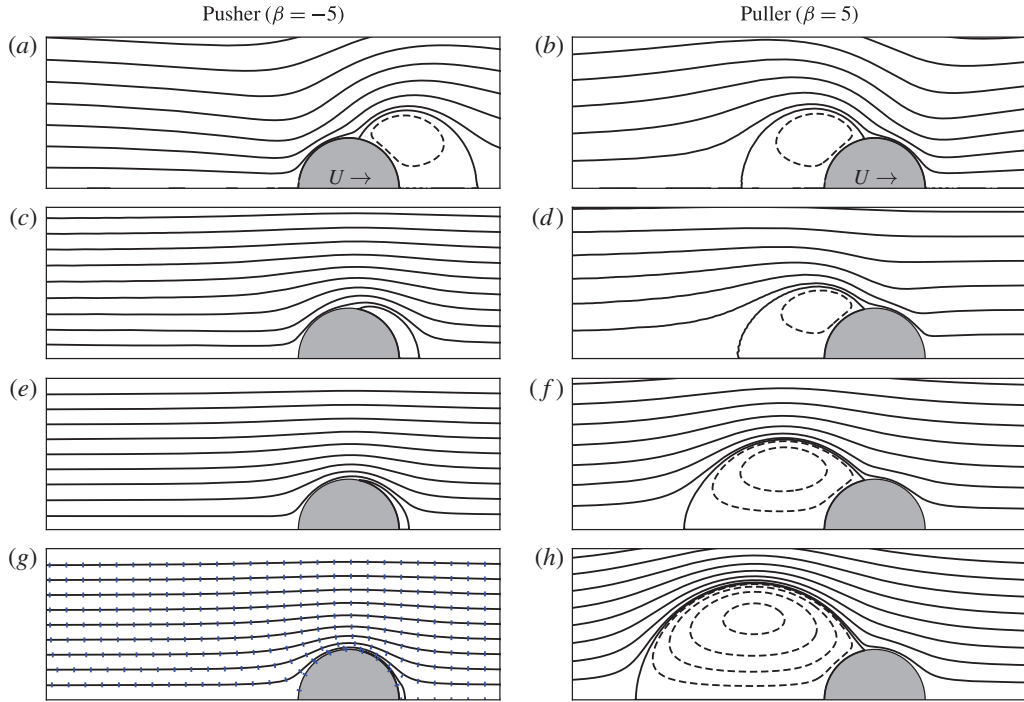


FIGURE 4. (Colour online) Streamlines of axisymmetric flow past a squirmer with  $\beta = \pm 5$ ; (a,c,e,g) pusher:  $\beta = -5$ , (b,d,f,h) puller:  $\beta = 5$ ;  $Re = 0.1$  (a,b), 10 (c,d), 100 (e,f), 1000 (g,h). Dashed streamlines represent negative values of the stream function. The tick marks in (g) at  $Re = 1000$  follow along streamlines of irrotational flow past a sphere.

The second term also vanishes if  $Re = 0$  due to the antisymmetric, purely diffusive, distribution of the vorticity, and it is hence associated with forces arising from the flow asymmetry produced by inertia at finite  $Re$ . Thus, (3.5) is satisfied identically in Stokes flow, and a squirmer propels itself at the same speed regardless of  $\beta$ . However, pushers increase in speed with  $Re$  while pullers decrease at finite  $Re \lesssim O(1)$ . In the former case, the first term represents a drag force because it is negative when  $\beta < 0$ . Thus, the redistribution of vorticity caused by inertia is responsible for the extra thrust that increases the swimming speed with  $Re$ . The opposite occurs for a puller, where  $\beta > 0$ : the contribution of the first term is a thrust, but it is outweighed by drag produced by the inertial redistribution of vorticity. As  $Re$  is increased beyond an  $O(1)$  value, the monotonic trend continues for a pusher until a limiting speed is reached. In contrast, the swimming speed of a puller becomes non-monotonic. A fuller explanation of these trends, especially when  $Re$  is large, requires a closer examination of the flow fields generated by squirmers and how they differ for pushers versus pullers.

#### 4.2. Flows generated by pushers and pullers

Streamlines illustrating the steady axisymmetric flow around pushers and pullers are shown in figures 4 and 5, and contours of constant vorticity are shown in figures 6 and 7. At  $Re = 0.1$ , symmetries in the near-field flow are apparent due to the dominance of viscous forces over inertial forces: reversing the sign of  $\beta$  causes the streamlines to be mirrored along the  $\rho$ -axis. Also, the vorticity is fore-aft

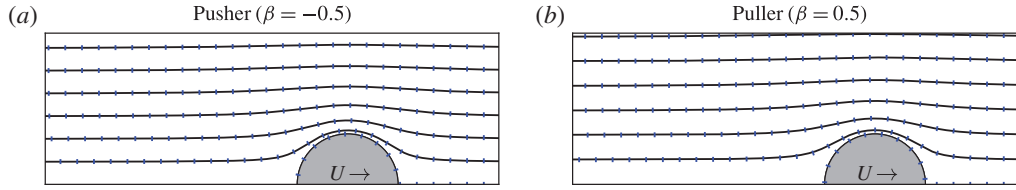


FIGURE 5. (Colour online) Similar to figure 4 except with  $\beta = \pm 0.5$ ; (a) pusher:  $\beta = -0.5$ ;  $Re = 1000$ , (b) puller:  $\beta = 0.5$ ;  $Re = 1000$ .

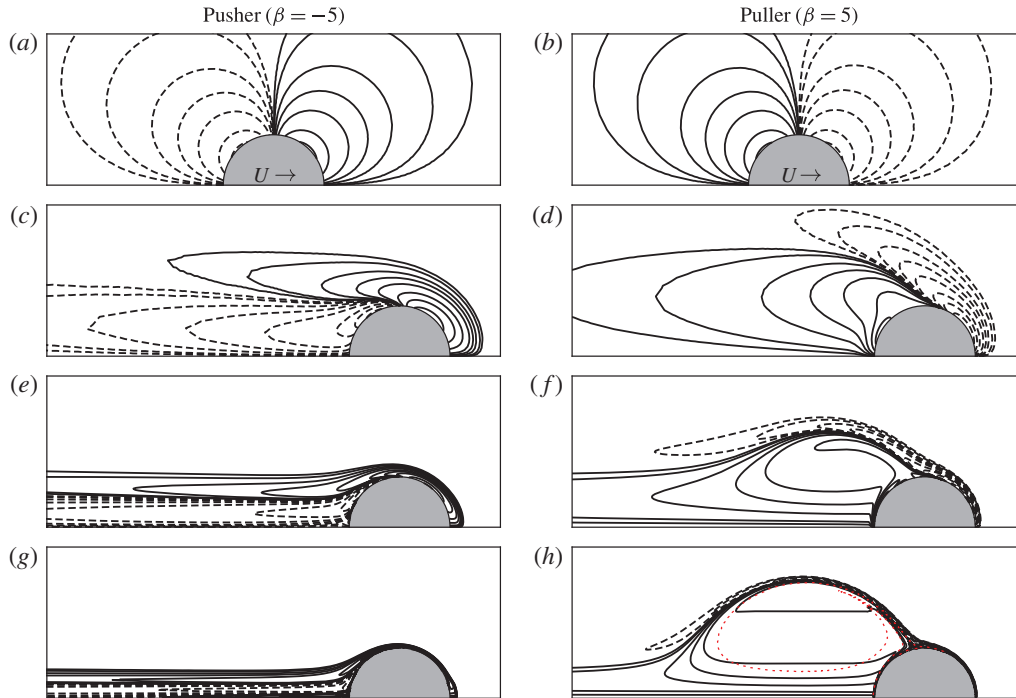


FIGURE 6. (Colour online) Vorticity contours for axisymmetric flow with  $\omega = \pm\{0.1, 0.2, 0.5, 1, 2, 5, \dots, 200\}$ . Dashed lines represent negative values. The dotted line in (h) at  $Re = 1000$  encircles the region where there is an approximately constant value of  $\omega/\rho = 2.9 \pm 0.05$ , indicating that the wake bubble behind a  $\beta = 5$  puller has a structure resembling a Hill's vortex; (a,c,e,g) pusher:  $\beta = -5$ , (b,d,f,h) puller:  $\beta = 5$ ;  $Re = 0.1$  (a,b), 10 (c,d), 100 (e,f), 1000 (g,h).

antisymmetric. Pushers generate positive vorticity ahead of their direction of travel and negative vorticity behind, while pullers do the opposite. Closed-streamline recirculatory regions appear in front of pushers and behind pullers if  $|\beta| > 1$ . Streamlines separate from the squirmer surface at the point where the stroke  $v_s(\theta)$  changes sign (Magar *et al.* 2003).

The flow patterns and swimming speed observed as  $Re$  is increased depend critically on  $\beta$ . For pushers at  $Re \gg 1$ , the majority of the vorticity, along with the upstream closed-streamline region that is present if  $\beta < -1$ , is concentrated into a laminar boundary layer of thickness  $O(1/\sqrt{Re})$ . This vorticity is then transported into a narrow downstream wake due to the motion of the swimming stroke (figures 6a,c,e,g

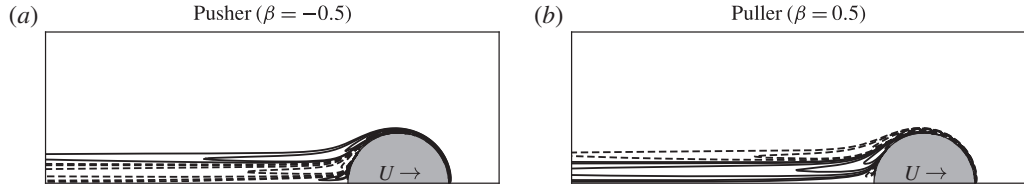


FIGURE 7. Similar to figure 6 except with  $\beta = \pm 0.5$ ; (a) pusher:  $\beta = -0.5$ ;  $Re = 1000$ , (b) puller:  $\beta = 0.5$ ;  $Re = 1000$ .

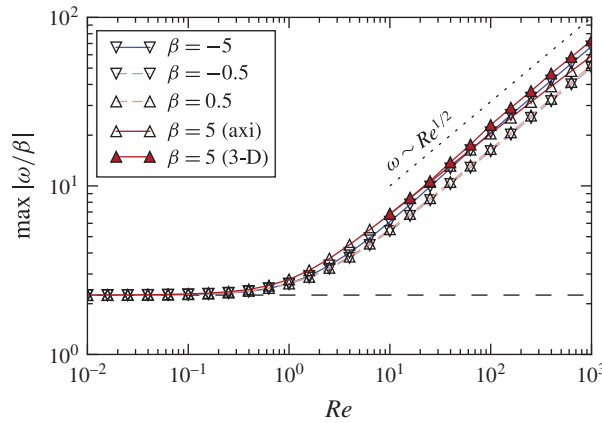


FIGURE 8. (Colour online) The maximum value of  $|\omega|$ , normalized by  $|\beta|$ , from axisymmetric computations at  $\beta = \pm 0.5$  and  $\pm 5$  and from 3-D computations for  $\beta = +5$ . In Stokes flow,  $\max |\omega/\beta| = 9|\beta|/4$ , as indicated by the dashed line to which the data collapses as  $Re \rightarrow 0$ . The dotted line indicates a slope of one-half, revealing that  $\omega \sim \sqrt{Re}$  at large  $Re$ .

and 7a). The streamlines outside the boundary layer and wake tend toward a potential flow profile, and no standing wake eddy is present (figures 4a,c,e,g and 5a). Thus, the flow around a pusher apparently resembles that past an inviscid spherical bubble at large  $Re_U$ , which exhibits the same characteristics (Moore 1963; Leal 1989). The key similarity is that the mobile surfaces of a bubble and a pusher squirmer cause advection of vorticity downstream, thus preventing it from accumulating into a recirculating wake. However, for a bubble, the shear-free surface produces  $\omega \sim O(1)$ , whereas for a squirmer,  $\omega \sim O(\sqrt{Re})$  in the boundary layer (figure 8) due to the fixed nature of the surface velocity profile (swimming stroke). This is akin to a towed, rigid sphere with a no-slip surface, where the greater amount of boundary layer vorticity results in flow separation and the appearance of a wake eddy if  $Re_U \gtrsim 10$ , which grows with  $Re_U$  (Dennis & Walker 1971; Fornberg 1988). These phenomena are avoided by a streamlined no-slip body, but for a pusher, the strong vorticity advection due to the propulsive surface motion interestingly achieves a similar effect. Despite the bluff body shape and  $O(\sqrt{Re})$  surface vorticity of a pusher, no wake eddy is produced.

The flow around pullers with  $0 < \beta < 1$  may be described likewise. As  $Re$  is increased, the boundary layer and wake become smaller in extent, and the majority of the flow domain becomes irrotational (figures 5b and 7b). Again, vorticity is



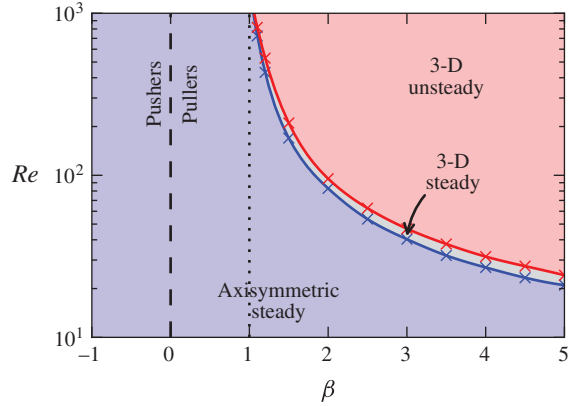


FIGURE 9. (Colour online) Flow state as a function of  $\beta$  and  $Re$ . The points of transition, marked with an ‘x’ and interpolated by the solid lines, were obtained numerically (see also table 1).

efficiently swept downstream by the mobile surface with a (monotonic) swimming stroke  $v_s(\theta)$  that is directed along the path of the flow. Consequently, pushers and pullers with  $\beta < 1$  reach a terminal (dimensionless) swimming speed (i.e. a dimensional swimming speed that is proportional to  $B_1$ ).

The axisymmetric flow that is observed around pullers with  $\beta > 1$  as  $Re$  increases is very different. A trailing vortical wake bubble is indeed present and grows with  $Re$  (figure 4*b,d,f,h*). Thus, for pullers with  $\beta > 1$ , the flow does not become irrotational within the majority of the flow domain as  $Re$  becomes large. As a result, the swimming speed of a  $\beta > 1$  squirmer does not attain a terminal value. The wake eddy is caused by the reversal of  $v_s$  along the rear half of the squirmer surface, which hinders the advection of vorticity downstream, and causes its accumulation behind the squirmer. This resembles flow past a rigid bluff body towed by an external force, where fluid deceleration along the no-slip surface has the same effect. Indeed, if the flow is restricted to be axisymmetric, the wake bubble resembles a Hill’s spherical vortex at  $Re = 1000$ , where  $\omega/\rho$  is constant in the region of closed streamlines and  $\omega = 0$  elsewhere (figure 6*h*). Batchelor (1956) proposed that such flow structures exist in the wake of bluff bodies in steady axisymmetric flow at large  $Re$ . The computations of Fornberg (1988) show the presence of a Hill’s vortex-like wake structure behind a sphere held fixed in a uniform flow, within which  $\omega/\rho$  is nearly constant once  $Re_U$  is sufficiently large. Moreover, it is shown that such large  $Re$  axisymmetric flows result in very low drag forces relative to that observed in 3-D flows beyond the onset of flow instabilities. The observation that  $U$  increases with  $Re$  for an axisymmetric  $\beta = 5$  pusher when  $Re \gtrsim O(1)$  (figure 3) indicates that the trailing vortex behind a  $\beta > 1$  puller is analogous to that behind a towed sphere; the wake eddy acts to decrease the overall drag. Note that the point of flow separation along the surface of a squirmer always occurs where  $v_s(\theta)$  changes sign regardless of  $Re$  (figure 4), whereas it depends on  $Re_U$  for a no-slip sphere.

#### 4.3. Transition to 3-D and unsteady flow

Figure 9 and table 1 detail the transition of the flow around a squirmer from steady and axisymmetric to unsteady and 3-D and are derived from unsteady 3-D flow



---

$\beta$	1.1	1.2	1.5	2.0	3.0	5.0
$Re^{(c1)}$	725	432	170	83.0	40.3	21.0
$Re^{(c2)}$	818	528	210	95.3	47.8	24.2
$Re^{(c2)} - Re^{(c1)}$	93	96	40	12.3	7.5	3.2

---

TABLE 1. Numerically obtained critical values of  $Re$  where the flow becomes 3-D ( $Re^{(c1)}$ ) and unsteady ( $Re^{(c2)}$ ) (see also figure 9).

---

simulations. The critical values of  $Re$  at which the axisymmetry breaks ( $Re^{(c1)}$ ) and at which the flow becomes unsteady ( $Re^{(c2)}$ ) are shown. For  $\beta > 1$  pullers,  $Re^{(c1)} < Re^{(c2)}$ , and a monotonic decrease of  $Re^{(c1)}$  and  $Re^{(c2)}$  with  $\beta$  is observed. Moreover,  $Re^{(c1)}$  and  $Re^{(c2)}$  both increase rapidly as  $\beta$  is decreased toward unity such that  $\beta = 1$  appears to be an asymptote; pushers and pullers with  $\beta < 1$  produce steady axisymmetric flows that remain stable up to at least  $Re = 1000$ .

This highlights another apparent similarity between the flow past a  $\beta < 1$  squirmer and an inviscid spherical bubble. For the latter, the asymptotic analysis of Moore (1963) suggested that a potential flow is recovered as  $Re_U \rightarrow \infty$ . Specific studies have also been carried out to determine how the wake structure and flow stability vary with aspect ratio for oblate spheroidal bubbles (Dandy & Leal 1986; Blanco & Magnaudet 1995; Magnaudet & Mougin 2007). It was revealed that only bubbles with an aspect ratio larger than 1.65 or 2.21 exhibit a standing wake eddy or an unstable wake, respectively. The reason is that a sufficient amount of vorticity (produced at the bubble surface in an amount proportional to the surface curvature) must accumulate in its wake for these transitions to occur. For a squirmer, a comparatively large  $O(\sqrt{Re})$  amount of boundary layer vorticity is generated, whereas it is  $O(1)$  for a spherical bubble, so the stability of the flow past pushers and  $\beta < 1$  pullers despite this fact is an intriguing result. Again, vorticity is strongly advected downstream by the propulsive surface velocity, preventing its accumulation in the wake, and the stability of the steady axisymmetric flow is preserved.

However, this does not imply stability at all  $Re$ . For no-slip objects where the vorticity is similarly  $O(\sqrt{Re})$ , turbulent boundary layers develop when  $Re$  is very large, even for streamlined objects such as airfoils or flat plates where there is no instability caused by a wake eddy. For example, the boundary layer of a no-slip sphere becomes turbulent at  $Re_U \approx 10^5$  (Deen 1998, p. 512). For this reason, it is very possible that the laminar boundary layer of a squirmer will also become turbulent at sufficiently large  $Re$ , except, perhaps, in the singular  $\beta = 0$  case where potential flow results identically. Such a phenomenon likely occurs well above the maximum  $Re = 1000$  considered in this work, and hence is not further discussed here.

Given the previously noted similarities of the steady axisymmetric flow around a  $\beta > 1$  puller to that past a no-slip sphere, one might expect that the transitions to 3-D and unsteady flows that occur will also be analogous. This indeed appears to be the case. For a no-slip sphere, the flow first bifurcates at  $Re_U^{(c1)} \approx 105$  (Natarajan & Acrivos 1993; Tomboulides & Orszag 2000), resulting in a steady 3-D flow that exhibits planar symmetry and two counter-rotating vortices in the wake. The symmetry plane passes through the axis of translation, but its orientation is arbitrary due to the initial axisymmetry of the flow. The scenario is the same for  $\beta > 1$  pullers, and planar flow symmetry is apparent in figure 10(a). The only difference is that  $Re^{(c1)}$  depends on  $\beta$  in the latter case. A second transition from steady to unsteady flow

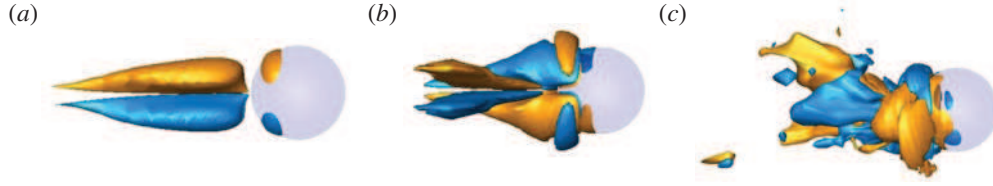


FIGURE 10. (Colour online) The streamwise component of the vorticity for a  $\beta = 5$  puller at an isocontour of  $\omega_z = \pm 1.05$ . In (a),  $Re = 22.6$ ; the flow is planar symmetric and steady ( $Re^{(c1)} < Re < Re^{(c2)}$ ). Two counter-rotating vortices are present in the wake. In (b),  $Re = 100$ ; the flow is also planar symmetric but unsteady ( $Re > Re^{(c2)}$ ), and the wake structure is more complicated; a pair of vortices is being shed downstream from the wake. Finally in (c),  $Re = 158$ ; the planar symmetry is broken and the flow appears to be almost chaotic in nature.

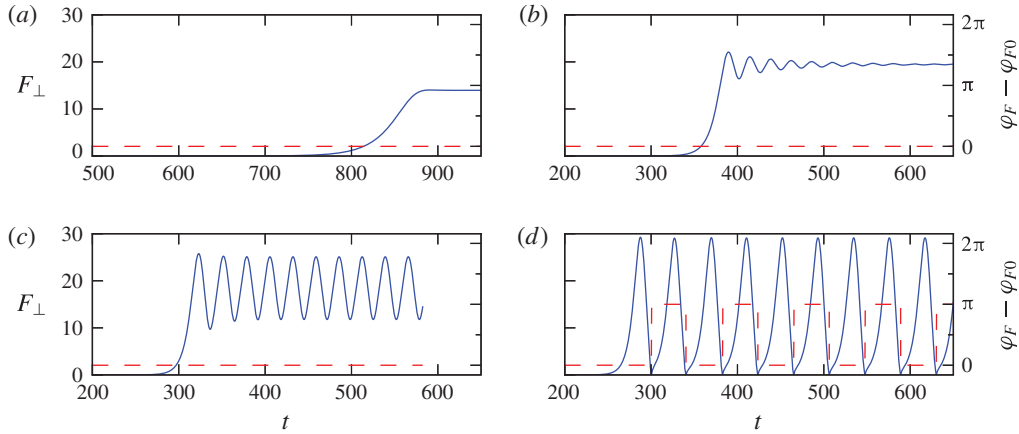


FIGURE 11. (Colour online) Magnitude of the lift force  $F_{\perp}$  normalized by  $2B_1a\mu/3$  (solid) and the azimuthal angle  $\varphi_F - \varphi_{F0}$  at which it acts (dashed) for a  $\beta = 5$  squirmer accelerating from rest at time  $t = 0$ . Time is normalized by  $3a/(2B_1)$ . Here,  $\varphi_{F0}$  represents the (arbitrary) initial angle of the lift when it first becomes non-zero. In (a)  $Re = 21.7$  and (b)  $Re = 24.0$ ,  $Re^{(c1)} < Re < Re^{(c2)}$ , and a constant steady-state lift force is observed. In (c)  $Re = 25.3$  and (d)  $Re = 26.7$ ,  $Re > Re^{(c2)}$ , and the lift force is oscillatory. In (c), the direction of the lift remains constant, while in (d) it periodically reverses direction.

takes place at  $Re_U^{(c2)} \approx 140$  in the case of a no-slip sphere (Natarajan & Acrivos 1993; Tomboulides & Orszag 2000), and the same happens for a  $\beta > 1$  puller at  $Re^{(c2)} = Re^{(c2)}(\beta)$ . In both cases, the planar flow symmetry persists, and as  $Re$  (or  $Re_U$ ) is further increased, shedding of the wake vortices begins to occur (figure 10b). Table 1 reveals that the quantity  $Re^{(c2)} - Re^{(c1)}$  decreases significantly as  $\beta$  is increased; the difference is approximately 40 at  $\beta = 1.5$  and decreases to only 3.2 at  $\beta = 5$ . The flow is more quickly destabilized when the value of  $\beta$  is larger, and hence there is only a narrow range of  $Re$  where it exhibits a steady 3-D state.

Once the flow enters an unsteady and/or 3-D state, the squirmer will no longer be force-free or torque-free in general. Examining the hydrodynamic forces and torques which arise in the vicinity of  $Re^{(c1)}$  and  $Re^{(c2)}$  yields some interesting observations. Figure 11 shows the lift, defined as the force perpendicular to the direction of

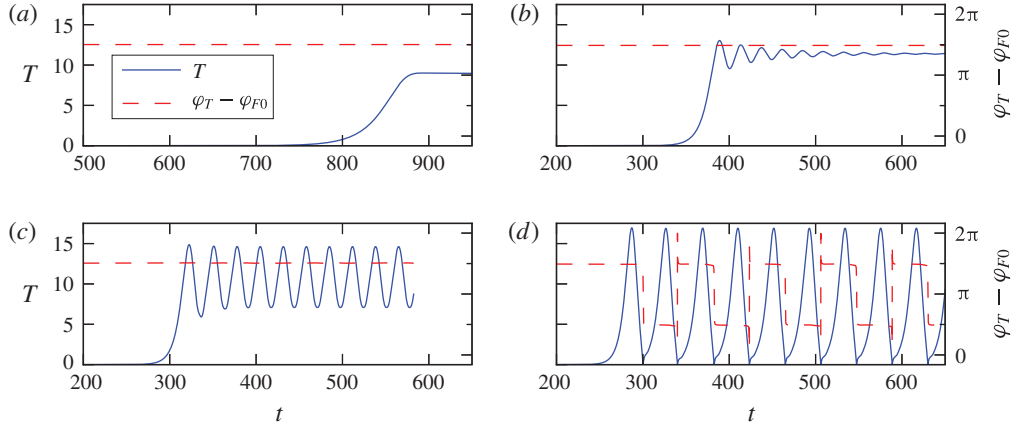


FIGURE 12. (Colour online) Analogous to figure 11 above, but now the magnitude of the hydrodynamic torque  $T$  (normalized by  $2B_1 a^2 \mu / 3$ ) is plotted along with the angle  $\varphi_T - \varphi_{F0}$  that the torque forms with the initial lift force;  $Re = 21.7$  (a),  $24.0$  (b),  $25.3$  (c),  $26.7$  (d). For all  $Re$  shown, the torque is perpendicular to both the direction of translation and the lift.

translation, for a  $\beta = 5$  puller started from rest, in which case  $Re^{(c1)} = 21.0$  and  $Re^{(c2)} = 24.2$ . If  $Re^{(c1)} < Re < Re^{(c2)}$ , as in (a,b), a constant lift force is generated once the flow reaches a steady state. Some small oscillations that eventually die out are observed at  $Re = 24.0$  but not at  $Re = 21.7$ . If  $Re > Re^{(c2)}$ , the flow is unsteady and hence the lift does not reach a constant value in figure 11(c,d). At  $Re = 25.3$ , the lift is oscillatory but always acts along the same direction, while at  $Re = 26.7$ , the lift periodically reverses direction. The torque generated on the squirmer, plotted in figure 12, clearly follows the same pattern as the lift, although it is offset by  $90^\circ$ . The lift and torque are perpendicular due to the planar flow symmetry; the lift is in the symmetry plane, while the torque is normal to it (the symmetry can be seen visually in figures 10a and 10b).

Hydrodynamic forces acting parallel to the direction of swimming also cause oscillations in the swimming speed when  $Re > Re^{(c2)}$ . The time-dependent speed of a  $\beta = 5$  puller accelerating from rest is shown in figure 13(a). Note that these oscillations have double the frequency of that in the lift and torque. It is also apparent that the average normalized swimming speed decreases significantly with increasing  $Re$ . This can be ascribed to vortex shedding; the drag-reducing effect of the vorticity-trapping wake bubble observed in (unstable) axisymmetric flows is lost as the vorticity is instead shed downstream. This explains the deviation of the unsteady 3-D simulations from the axisymmetric ones seen in figure 3 at approximately the same point at which the flow becomes unsteady.

From the dominant dimensional frequency  $f$  of the oscillations in the lift force, we define the Strouhal number as  $St = 3fa / (2B_1)$ , which is plotted for a  $\beta = 5$  puller in figure 13(b). A rapid initial decrease of  $St$  occurs just as  $Re$  exceeds  $Re^{(c2)}$  and unsteady flow is established. At slightly higher  $Re$ ,  $St$  rebounds and maintains a value between 0.024 and 0.029 between  $Re = 60$  and  $Re = 160$ . This can be roughly compared to flow past a no-slip sphere where  $St_U = fa / U = 0.067$  at  $Re_U = 150$  (Natarajan & Acrivos 1993; Tomboulides & Orszag 2000).

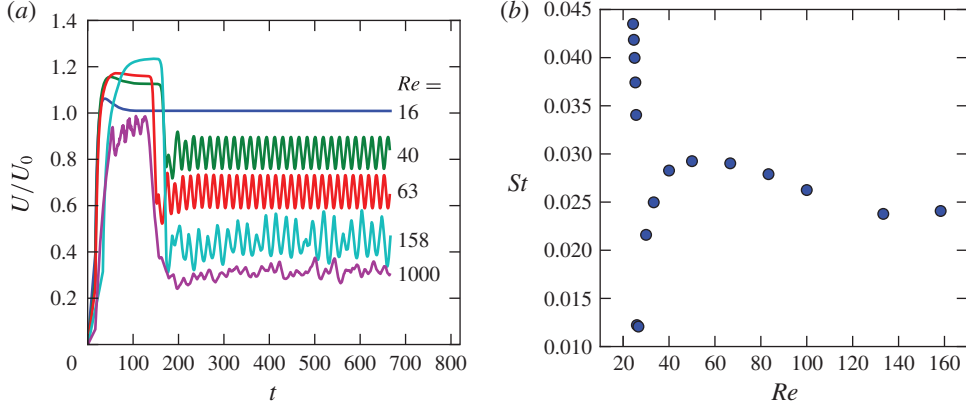


FIGURE 13. (Colour online) (a) Swimming speed,  $U/U_0$  versus time,  $t$ , for a  $\beta = 5$  puller accelerating from rest (3-D simulation). Time is normalized by  $3a/(2B_1)$ . (b) The Strouhal number  $St$  versus  $Re$  for a  $\beta = 5$  puller.

It is also apparent from figure 13(a) that the flow at  $\beta = 5$  transitions from having just a single frequency at  $Re = 63$  to appearing nearly chaotic at  $Re = 158$ . Also, the planar symmetry observed at  $Re = 100$  (figure 10b) is clearly broken at  $Re = 158$  (figure 10c). Similar transitions occur for flow past a no-slip sphere in the range  $300 < Re_U < 500$ , and the fluctuations in the flow become increasingly irregular as  $Re$  is further increased, signifying the beginnings of turbulence (Tomboulides & Orszag 2000). This is also observed for a  $\beta = 5$  puller at  $Re = 1000$ , as the increasingly chaotic nature of the flow causes increasingly broadband fluctuations in the swimming speed.

#### 4.4. Power expenditure and hydrodynamic efficiency

The dimensionless power  $\mathcal{P}$  expended by a squirmer versus  $Re$  for  $\beta = 0, \pm 0.5$  and  $\pm 5$  is shown in figure 14(a). This is calculated as the rate of work done on the fluid by the tangential motion of the squirmer surface,

$$\mathcal{P} = - \int_S \mathbf{n} \cdot \boldsymbol{\sigma} \cdot (v_s \mathbf{e}_\theta) dS, \quad (4.1)$$

where  $\mathcal{P}$  is normalized by  $4B_1^2 a \mu / 9$ . In axisymmetric flow, (4.1) simplifies to

$$\mathcal{P} = 2\pi \int_0^\pi (2v_s - \omega|_{r=1}) v_s \sin \theta d\theta. \quad (4.2)$$

Additionally, power expended by the squirmer is dissipated viscously by the fluid. The dimensionless rate of viscous dissipation  $\Phi$  in the flow around a tangentially deforming spherical body can be given in terms of the vorticity and surface velocity (Stone 1993; Stone & Samuel 1996),

$$\Phi = \int_V \boldsymbol{\sigma} : \nabla \mathbf{v} dV = \int_V \boldsymbol{\omega} \cdot \boldsymbol{\omega} dV + 2 \int_S v_s^2 dS, \quad (4.3)$$

and at steady state,  $\Phi = \mathcal{P}$ . This implies that a squirmer that minimizes the amount of vorticity that it generates in the fluid will also minimize its power expenditure.

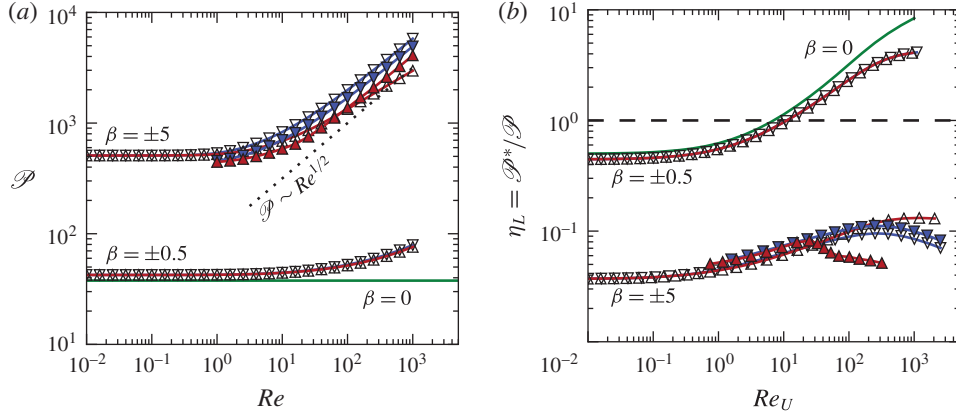


FIGURE 14. (Colour online) Power  $\mathcal{P}$  expended by a squirmer versus  $Re$  (a), and the Lighthill efficiency  $\eta_L$  versus the translational Reynolds number  $Re_U = \rho Ua/\mu$  (b). Here,  $\mathcal{P}^*$  is the power necessary to tow a sphere in steady axisymmetric flow. A neutral ( $\beta = 0$ ) squirmer is indicated by the solid line (with no markers) and has  $\mathcal{P} = 12\pi$  at all  $Re$ .

In fact, a neutral ( $\beta = 0$ ) squirmer expends the least amount of energy at all  $Re$  since it generates no vorticity. In this case, integrating (4.2) gives  $\mathcal{P}|_{\beta=0} = 12\pi$  for all  $Re$ . We may also integrate (4.2) to give the power expenditure in Stokes flow,  $\mathcal{P}|_{Re=0} = 12\pi(2 + \beta^2)/2$  (Wang & Ardekani 2012), which gives the limits approached by the data in figure 14(a) as  $Re \rightarrow 0$ . As  $Re$  is increased,  $\mathcal{P}$  increases (if  $\beta \neq 0$ ) due to increased vorticity generation. As shown in figure 8,  $|\omega|_{max}$  increases monotonically, scaling with  $\sqrt{Re}$  within the boundary layer at large  $Re$ . From (4.2) and (4.3), we expect the same scaling for  $\mathcal{P}$ , which is indeed observed in figure 14(a). We also observe that  $\mathcal{P}(\beta, Re) > \mathcal{P}(\beta, 0)$  for all  $Re > 0$ . One might conjecture that this behaviour is predicted by the Helmholtz minimum dissipation theorem (Batchelor 1967), which guarantees that a Stokes flow field dissipates less energy than any other incompressible flow field with the same boundary velocities. However, the far-field boundary velocity for a squirmer is given by its swimming speed  $U$ , which generally depends on  $Re$ , so the theorem does not apply. Nonetheless, the observation that  $\mathcal{P}$  is minimized at  $Re = 0$  for a given value of  $\beta$  is intriguing. Moreover, we observe that  $\mathcal{P}$  increases monotonically with  $Re$ . This finding may be compared to the monotonic increase of the extensional viscosity of a dilute suspension of rigid spheres with  $Re$  in uniaxial extensional flow. Specifically, the extensional viscosity also increases monotonically and scales with  $\sqrt{Re}$  at large  $Re$  due to intense  $O(\sqrt{Re})$  boundary layer vorticity (Ryskin 1980). The extensional viscosity is proportional to the viscous dissipation rate in the flow. Thus, it is an interesting observation that the power expended by a squirmer, which is viscously dissipated, behaves similarly to the extensional viscosity of a dilute suspension of spheres as a function of the Reynolds number.

The Lighthill (1952) efficiency  $\eta_L$  of a squirmer is defined as the ratio of the power  $\mathcal{P}^*$  required to tow a no-slip sphere at a speed  $U$  to the power  $\mathcal{P}$  expended by a squirmer to swim at that same speed. This quantity is plotted in figure 14(b). Here, the horizontal axis is the Reynolds number based on the translational swimming speed,  $Re_U = ReU = \rho Ua/\mu$ . Note that we take  $\mathcal{P}^*$  as the power required to tow a sphere in steady axisymmetric flow at the same  $Re_U$ . At  $Re = 0$ ,  $\eta_L = 1/(2 + \beta^2)$ ,

pushers and pullers have the same efficiency. At small  $Re$ , asymptotic theory shows that pushers are slightly more efficient than pullers (Wang & Ardekani 2012). Thus, it would be reasonable to expect that larger differences in efficiency might be observed at larger  $Re$ . Interestingly, our results reveal that the difference in efficiency between a  $\beta = \pm 0.5$  pusher and puller is very slight, even up to  $Re = 1000$ . This is somewhat surprising considering that a  $\beta = -0.5$  pusher moves nearly 10% faster than a  $\beta = 0.5$  puller at  $Re = 1000$ . Thus, in this case, a puller and pusher exert approximately the same amount of power once differences in speed are taken into account. Similarly, a  $\beta = \pm 5$  puller and pusher have nearly the same efficiency up to the point where the steady axisymmetric flow destabilizes at  $Re_U \approx 20$ , with that of a pusher being only slightly greater. If one considers the unstable axisymmetric flow that arises beyond  $Re_U \approx 20$ , pullers interestingly become more efficient than pushers. The drag reducing effect of the Hill's vortex-like wake is responsible. However, if the flow is allowed to be unsteady and 3-D, pushers continue to be more efficient by a margin that increases with  $Re_U$ . The vortex shedding that takes place in the wake of a high  $Re$  puller reduces the amount of swimming work that goes into forward propulsion and causes a subsequent loss of efficiency. This suggests that 'pushing' may be more efficient than 'pulling' at larger  $Re$  due to the increased flow stability.

One may notice that  $\eta_L$  increases above unity in some cases, indicating that the power required to tow a sphere exceeds that expended by a squirmer swimming at the same speed. In Stokes flow,  $\eta_L \leq 3/4$  for any spherical swimmer moving only by tangential surface deformations (Stone & Samuel 1996). For a neutral squirmer at  $Re = 0$ ,  $\eta_L = 1/2$ . However, this bound does not apply when  $Re > 0$ . Indeed,  $\eta_L|_{\beta=0}$  increases above unity at  $Re_U \approx 7$ , and the same is true for  $\beta = \pm 0.5$  squirmers at  $Re_U \approx 10$ . This highlights the difficulty of swimming against wholly resistive viscous forces (Purcell 1977). For a squirmer, swimming is always less efficient than being towed by an external force in the absence of fluid inertia, but may be more efficient when inertia is present.

Finally, we note that the propulsion of a squirmer via tangential surface motion is drag-based. This is in contrast to the flapping and undulatory mechanisms of propulsion employed by some (usually large  $Re$ ) swimmers such as fishes, which are lift-based. The efficiency of lift-based propulsion can be very high in inertial flows where  $Re$  is large. However, this efficiency decreases drastically with  $Re$ , and drag-based propulsion has superior efficiency when fluid viscosity is a strong factor (Walker 2002). Thus, without rigorous calculation, we surmise that the efficiency of a squirmer improves compared to lift-based propulsion as  $Re$  is decreased, likely being comparable at moderate  $Re$ . This clearly makes sense from a biological perspective; the ciliated organisms most closely described by the squirmer model are often microorganisms that swim at small  $Re$ , although ctenophores provide an interesting example of moderate to large  $Re$  squirmers.

## 5. Conclusion

We have demonstrated fundamental differences between the locomotions of pusher and puller squirmers with a fixed swimming stroke when inertia is important to the flow. Specifically, it is shown that a pusher, as well as a  $\beta < 1$  puller, does not generate a standing wake eddy, and also that it produces steady axisymmetric flow that remains stable to at least  $Re = 1000$ . The vorticity is confined to a laminar boundary layer of thickness  $O(\sqrt{Re})$ , and the flow becomes largely irrotational as  $Re$  increases.



This is due to the strong downstream advection of vorticity by the propulsive surface velocity profile. Before, such behaviour had only been demonstrated for bubbles, which produce  $O(1)$  vorticity. That this also holds for a  $\beta < 1$  squirmer is a key result, as squirmers produce a much larger  $O(\sqrt{Re})$  vorticity (similar to a no-slip body).

In contrast, a  $\beta > 1$  puller is ineffective at transporting vorticity from its wake, similar to a towed, rigid sphere. Thus, it exhibits a recirculating wake region that triggers a transition to unsteady 3-D flow at a critical  $Re$ . A progression of flow patterns is observed as  $Re$  is further increased, which strongly resemble those that occur for a rigid sphere, until weakly turbulent flow develops when  $Re \sim O(1000)$ .

Finally, we show that squirmers that minimize vorticity generation generally maximize their efficiency. In the range of  $Re$  where steady axisymmetric flow is stable, the swimming efficiency of pushers and pullers is surprisingly similar. However, the vortex shedding that occurs for  $\beta > 1$  pullers in unsteady 3-D flow at larger  $Re$  reduces their overall efficiency below that of a pusher where the axisymmetric flow remains stable.

Future work will entail further quantification of squirmers in unsteady 3-D flows; at sufficiently large  $Re$ , the flow around  $\beta > 1$  pullers is expected to become fully turbulent, similar to flow around a no-slip body. Furthermore, it would be worthwhile to consider the motion of squirmers that are not bound to move along a single axis of translation. In this case, the motion of the squirmer would be fully coupled to the flow, and different swimming paths would be observed depending upon the values of  $Re$  and  $\beta$ . The present results will be useful in quantifying fluid mixing, production of feeding currents and hydrodynamic signalling by the abundance of aquatic swimmers living at  $Re$  up to 1000.

### Acknowledgements

This work was funded in part by the European Union through a CIG grant to E.L. N.G.C. acknowledges partial support from the John and Claire Bertucci Fellowship in Engineering. The freely licensed software libraries NumPy, SciPy (Jones, Oliphant & Peterson 2015) and Matplotlib (Hunter 2007) were used in producing many of the results and figures presented in this article.

### Appendix. Validation of numerical solutions

Convergence of the flow computations with respect to the grid parameters was tested empirically. First, it was ensured that the distance  $R_\infty$  from the squirmer at which uniform flow was imposed was large enough to not affect the computed swimming speed  $U$ . Computations were relatively insensitive to this parameter due to the fast velocity decay from the squirmer surface ( $\sim 1/r^2$  at  $Re = 0$  and  $\sim 1/r^3$  at large  $Re$ , outside the wake) (Subramanian 2010), provided that the domain was not so small as to restrict flow near the squirmer body. For the axisymmetric computations, the polynomial order  $N$  of the shape functions within each element was incrementally increased to convergence (figure 15). In order to fully resolve the boundary layer, it was ensured that the condition  $\Delta_{r0}/\delta \lesssim N^2/9$  (Gottlieb & Orszag 1977) was satisfied, where  $\Delta_{r0}$  is the element size (perpendicular to the boundary layer) and  $\delta$  is the boundary layer thickness. The thickness of the boundary layer was estimated as  $\delta = O(1/\sqrt{Re})$  since the boundary layer is expected to be laminar. For the second-order accurate finite-volume method used for 3-D computations, a higher mesh resolution is



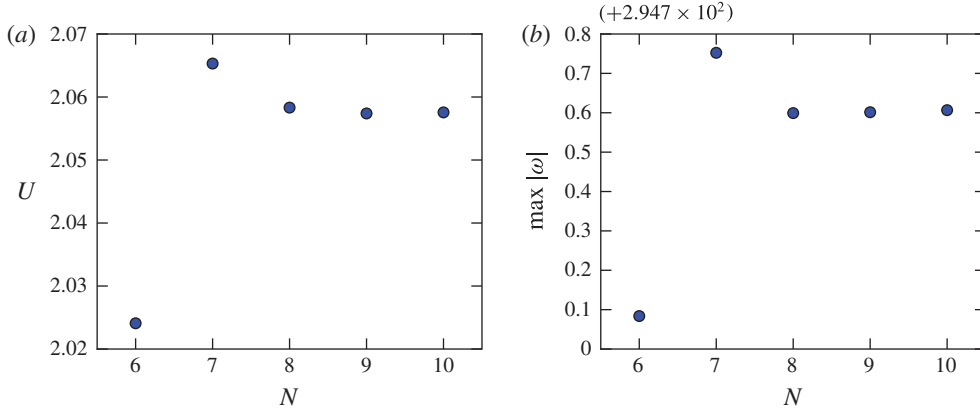


FIGURE 15. (Colour online) Convergence of the swimming speed  $U$  (a) and  $\max |\omega|$  (b) for a  $\beta = 5$  puller at  $Re = 1000$  computed via a spectral element method for steady axisymmetric flow. The horizontal axis represents the degree of the shape functions within each element. The element thickness in the boundary layer was  $\Delta_{r0} = 0.01$ .

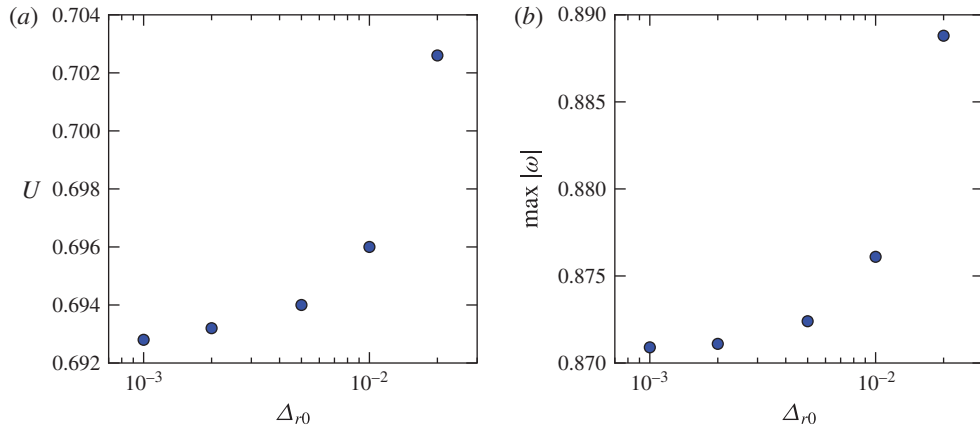


FIGURE 16. (Colour online) Convergence of the swimming speed  $U$  (a) and  $\max |\omega|$  (b) with respect to the grid resolution at the squirmer surface for 3-D unsteady flow computed via a second-order accurate finite-volume method. Here,  $\beta = -0.5$  and  $Re = 1$ .

required due to the lower order approximation, and satisfactorily converged solutions were reached with  $\Delta_{r0} = 0.001$  (figure 16).

Additional validation of our computational methods was carried out by computing the drag coefficient of a no-slip sphere in uniform flow and comparing to previously known results (figure 17). The drag coefficient is defined as  $C_D = 2F_D/(\pi \rho a^2 U^2)$ , where  $F_D$  is the drag force and  $U$  is the far-field velocity of the oncoming flow. Known values are provided by the correlation  $C_D = (\sqrt{12/Re_U} + 0.5407)^2$  (Abraham 1970). Additionally, values in (potentially unstable) steady axisymmetric flow up to  $Re_U = 2500$  are provided by Fornberg (1988). The computational meshes used for our computations were the same as those used for the squirmer computations at  $Re = 1000$ . The results of the comparison show good agreement. Note that when  $Re_U \gtrsim 500$ ,  $C_D$  becomes nearly constant, and the reported computations reproduce this feature.

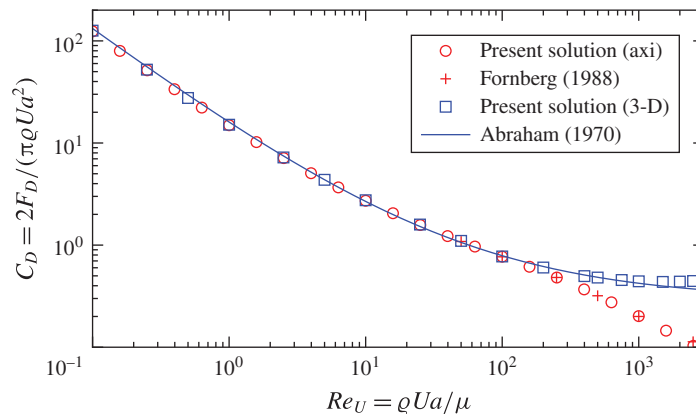


FIGURE 17. (Colour online) The drag coefficient  $C_D$  of a no-slip sphere in uniform flow computed using the numerical methods described in § 3. Comparison is made to the results of Fornberg (1988) (for steady axisymmetric flow) and the correlation given by Abraham (1970).

#### REFERENCES

- ABRAHAM, F. F. 1970 Functional dependence of drag coefficient of a sphere on Reynolds number. *Phys. Fluids* **13** (8), 2194–2195.
- AFANASYEV, Y. D. 2004 Wakes behind towed and self-propelled bodies: asymptotic theory. *Phys. Fluids* **16**, 3235–3238.
- BATCHELOR, G. K. 1956 A proposal concerning laminar wakes behind bluff bodies at large Reynolds number. *J. Fluid Mech.* **1** (04), 388–398.
- BATCHELOR, G. K. 1967 *An Introduction to Fluid Mechanics*. Cambridge University Press.
- BATCHELOR, G. K. 1970 The stress system in a suspension of force-free particles. *J. Fluid Mech.* **41**, 545–570.
- BLAKE, J. R. 1971 A spherical envelope approach to ciliary propulsion. *J. Fluid Mech.* **46**, 199–208.
- BLANCO, A. & MAGNAUDET, J. 1995 The structure of the axisymmetric high-Reynolds number flow around an ellipsoidal bubble of fixed shape. *Phys. Fluids* **7** (6), 1265–1274.
- BRENNEN, C. & WINNET, H. 1977 Fluid mechanics of propulsion by cilia and flagella. *Annu. Rev. Fluid Mech.* **9**, 339–398.
- CHILDRESS, S. 1981 *Mechanics of Swimming and Flying*. Cambridge University Press.
- DANDY, D. S. & LEAL, L. G. 1986 Boundary-layer separation from a smooth slip surface. *Phys. Fluids* **29** (5), 1360–1366.
- DEEN, W. M. 1998 *Analysis of Transport Phenomena*. Oxford University Press.
- DENNIS, S. C. R. & WALKER, J. D. A. 1971 Calculation of the steady flow past a sphere at low and moderate Reynolds numbers. *J. Fluid Mech.* **48** (04), 771–789.
- DRESCHER, K., LEPTOS, K. C. C., TUVAL, I. & ISHIKAWA, T. 2009 Dancing Volvox: Hydrodynamic bound states of swimming algae. *Phys. Rev. Lett.* **102**, 168101.
- ERN, P., RISSO, F., FABRE, D. & MAGNAUDET, J. 2012 Wake-induced oscillatory paths of bodies freely rising or falling in fluids. *Annu. Rev. Fluid Mech.* **44**, 97–121.
- FABRE, D., AUGUSTE, F. & MAGNAUDET, J. 2008 Bifurcations and symmetry breaking in the wake of axisymmetric bodies. *Phys. Fluids* **20** (5), 051702.
- FORNBERG, B. 1988 Steady viscous flow past a sphere at high Reynolds numbers. *J. Fluid Mech.* **190**, 471–489.
- GAZZOLA, M., VAN REES, W. M. & KOUMOUTSAKOS, P. 2012 C-start: optimal start of larval fish. *J. Fluid Mech.* **698**, 5–18.
- GEUZAIN, C. & REMACLE, J.-F. 2009 Gmsh: A 3-D finite element mesh generator with built-in pre-and post-processing facilities. *Intl J. Numer. Meth. Engng* **79** (11), 1309–1331.

- GOTTLIEB, D. & ORSZAG, S. A. 1977 *Numerical Analysis of Spectral Methods: Theory and Applications*. vol. 26. SIAM.
- GRAY, J. 1968 *Animal Locomotion*. Weidenfeld & Nicolson.
- HALLEZ, Y. & LEGENDRE, D. 2011 Interaction between two spherical bubbles rising in a viscous liquid. *J. Fluid Mech.* **673**, 406–431.
- HAMEL, A., FISCH, C., COMBETTES, L., DUPUIS-WILLIAMS, P. & BAROUD, C. N. 2011 Transitions between three swimming gaits in paramecium escape. *Proc. Natl Acad. Sci. USA* **108** (18), 7290–7295.
- HOROWITZ, M. & WILLIAMSON, C. H. K. 2010 The effect of Reynolds number on the dynamics and wakes of freely rising and falling spheres. *J. Fluid Mech.* **651**, 251–294.
- HUNTER, J. D. 2007 Matplotlib: A 2D graphics environment. *Comput. Sci. Engng* **9** (3), 90–95.
- ISHIKAWA, T., SIMMONDS, M. P. & PEDLEY, T. J. 2006 Hydrodynamic interaction of two swimming model micro-organisms. *J. Fluid Mech.* **568**, 119–160.
- ISHIKAWA, T., SIMMONDS, M. P. & PEDLEY, T. J. 2007 The rheology of a semi-dilute suspension of swimming model micro-organisms. *J. Fluid Mech.* **588**, 399–435.
- JOHNSON, T. A. & PATEL, V. C. 1999 Flow past a sphere up to a Reynolds number of 300. *J. Fluid Mech.* **378**, 19–70.
- JONES, E., OLIPHANT, T. & PETERSON, P. 2015 SciPy: Open source scientific tools for Python. Available at [www.scipy.org](http://www.scipy.org).
- JORDAN, C. E. 1992 A model of rapid-start swimming at intermediate Reynolds number: undulatory locomotion in the chaetognath *Sagitta elegans*. *J. Expl Biol.* **163** (1), 119–137.
- KARNIADAKIS, G. E. & SHERWIN, S. 2005 *Spectral/hp Element Methods for Computational Fluid Dynamics*, 2nd edn. Oxford University Press.
- KERN, S. & KOUMOUTSAKOS, P. 2006 Simulations of optimized anguilliform swimming. *J. Expl Biol.* **209**, 4841–4857.
- KHAIR, A. S. & CHISHOLM, N. G. 2014 Expansions at small Reynolds numbers for the locomotion of a spherical squirmer. *Phys. Fluids* **26**, 011902.
- LAUGA, E. & POWERS, T. R. 2009 The hydrodynamics of swimming microorganisms. *Rep. Prog. Phys.* **72**, 096601.
- LEAL, L. G. 1989 Vorticity transport and wake structure for bluff bodies at finite Reynolds number. *Phys. Fluids A* **1** (1), 124–131.
- LEGENDRE, D. & MAGNAUDET, J. 1998 The lift force on a spherical body in a viscous linear shear flow. *J. Fluid Mech.* **368**, 81–126.
- LEGENDRE, D., MERLE, A. & MAGNAUDET, J. 2006 Wake of a spherical bubble or a solid sphere set fixed in a turbulent environment. *Phys. Fluids* **18** (4), 048102.
- LI, G.-J. & ARDEKANI, A. M. 2014 Hydrodynamic interaction of microswimmers near a wall. *Phys. Rev. E* **90**, 013010.
- LIGHTHILL, M. J. 1952 On the squirming motion of nearly spherical deformable bodies through liquids at very small Reynolds numbers. *Commun. Pure Appl. Maths* **5**, 109–118.
- LIGHTHILL, M. J. 1975 *Mathematical Biofluidynamics*. SIAM.
- LIN, Z., THIFFEAULT, J.-L. & CHILDRESS, S. 2011 Stirring by squirmers. *J. Fluid Mech.* **669**, 167–177.
- LLOPIS, I. & PAGONABARRAGA, I. 2010 Hydrodynamic interactions in squirmer motion: Swimming with a neighbour and close to a wall. *J. Non-Newtonian Fluid Mech.* **165** (17–18), 946–952.
- MAGAR, V., GOTO, T. & PEDLEY, T. J. 2003 Nutrient uptake by a self-propelled steady squirmer. *Q. J. Mech. Appl. Maths* **56**, 65–91.
- MAGAR, V. & PEDLEY, T. J. 2005 Average nutrient uptake by a self-propelled unsteady squirmer. *J. Fluid Mech.* **539**, 93–112.
- MAGNAUDET, J. & MOUGIN, G. 2007 Wake instability of a fixed spheroidal bubble. *J. Fluid Mech.* **572**, 311–337.
- MAGNAUDET, J., RIVERO, M. & FABRE, J. 1995 Accelerated flows past a rigid sphere or a spherical bubble. Part 1. Steady straining flow. *J. Fluid Mech.* **284**, 97–135.
- MATSUMOTO, G. I. 1991 Swimming movements of ctenophores, and the mechanics of propulsion by ctenophore rows. *Hydrobiologia* **216–217** (1), 319–325.

- MCHENRY, M. J., AZIZI, E. & STROTHER, J. A. 2003 The hydrodynamics of locomotion at intermediate Reynolds numbers: undulatory swimming in ascidian larvae (*Botrylloides sp.*). *J. Expl Biol.* **206** (2), 327–343.
- MERLE, A., LEGENDRE, D. & MAGNAUDET, J. 2005 Forces on a high-*Re* spherical bubble in a turbulent flow. *J. Fluid Mech.* **532**, 53–62.
- MICHELIN, S. & LAUGA, E. 2011 Optimal feeding is optimal swimming for all Peclet numbers. *Phys. Fluids* **23** (10), 101901.
- MOORE, D. W. 1963 The boundary layer on a spherical gas bubble. *J. Fluid Mech.* **16** (02), 161–176.
- MOUGIN, G. & MAGNAUDET, J. 2001 Path instability of a rising bubble. *Phys. Rev. Lett.* **88** (1), 014502.
- NATARAJAN, R. & ACRIVOS, A. 1993 The instability of the steady flow past spheres and disks. *J. Fluid Mech.* **254**, 323–344.
- PAK, O. S. & LAUGA, E. 2016 Theoretical models of low-Reynolds-number locomotion. In *Fluid-Structure Interactions in Low-Reynolds-Number Flows* (ed. C. Duprat & H. Stone), chap. 4, pp. 100–167. The Royal Society of Chemistry.
- PURCELL, E. M. 1977 Life at low Reynolds number. *Am. J. Phys.* **45**, 3–11.
- PUSHKIN, D. O., SHUM, H. & YEOMANS, J. M. 2013 Fluid transport by individual microswimmers. *J. Fluid Mech.* **726**, 5–25.
- RYSKIN, G. 1980 The extensional viscosity of a dilute suspension of spherical particles at intermediate microscale Reynolds numbers. *J. Fluid Mech.* **99** (03), 513–529.
- STONE, H. A. 1993 An interpretation of the translation of drops and bubbles at high Reynolds numbers in terms of the vorticity field. *Phys. Fluids A* **5** (10), 2567–2569.
- STONE, H. A. & SAMUEL, A. D. T. 1996 Propulsion of microorganisms by surface distortions. *Phys. Rev. Lett.* **77**, 4102–4104.
- SUBRAMANIAN, G. 2010 Viscosity-enhanced bio-mixing of the oceans. *Curr. Sci.* **98** (8), 1103–1108.
- TAMM, S. L. 2014 Cilia and the life of ctenophores. *Invertebr. Biol.* **133** (1), 1–46.
- THIFFEAULT, J.-L. & CHILDRESS, S. 2010 Stirring by swimming bodies. *Phys. Lett. A* **374** (34), 3487–3490.
- TOMBOULIDES, A. G. & ORSZAG, S. A. 2000 Numerical investigation of transitional and weak turbulent flow past a sphere. *J. Fluid Mech.* **416**, 45–73.
- TYTELL, E. D., HSU, C.-Y., WILLIAMS, T. L., COHEN, A. H. & FAUCI, L. J. 2010 Interactions between internal forces, body stiffness, and fluid environment in a neuromechanical model of lamprey swimming. *Proc. Natl Acad. Sci. USA* **107** (46), 19832–19837.
- VOGEL, S. 1996 *Life in Moving Fluids*. Princeton University Press.
- WALKER, J. A. 2002 Functional morphology and virtual models: physical constraints on the design of oscillating wings, fins, legs, and feet at intermediate Reynolds numbers. *Integr. Comp. Biol.* **42** (2), 232–242.
- WANG, S. & ARDEKANI, A. 2012 Inertial squirmer. *Phys. Fluids* **24**, 101902.
- ZHU, L., DO-QUANG, M., LAUGA, E. & BRANDT, L. 2011 Locomotion by tangential deformation in a polymeric fluid. *Phys. Rev. E* **83** (1), 011901.
- ZHU, L., LAUGA, E. & BRANDT, L. 2012 Self-propulsion in viscoelastic fluids: pushers versus pullers. *Phys. Fluids* **24** (5), 091902.